



Uncovering the pathway of peroxymonosulfate activation over $\text{Co}_{0.5}\text{Zn}_{0.5}\text{O}$ nanosheets for singlet oxygen generation: Performance and membrane application

Xiaoke Zhang^a, Jin Liu^{b,*}, Hongzhong Zhang^c, Zhen Wan^d, Jun Li^{a,*}

^a Henan Institute of Advanced Technology, Zhengzhou University, Zhengzhou 450052, PR China

^b Henan Key Laboratory of Rare Earth Functional Materials, Zhoukou Normal University, Zhoukou 466001, PR China

^c School of Materials and Chemical Engineering, Zhengzhou University of Light Industry, Zhengzhou 450001, PR China

^d Key Laboratory of Catalysis and Materials Science of the State Ethnic Affairs Commission and Ministry of Education, College of Resources and Environmental Science, South-Central Minzu University, Wuhan 430074, PR China

ARTICLE INFO

Keywords:

Solid solution
Peroxymonosulfate activation
Membrane technology
Non-radical pathway
Singlet oxygen

ABSTRACT

Singlet oxygen ($^1\text{O}_2$) exhibits excellent activity for degradation of refractory pollutants and strong resistance in a wide pH range and harsh environment. The efficient generation of reactive oxygen species is vital for the treatment of wastewater in peroxymonosulfate (PMS) system, but how to boost the selectivity of $^1\text{O}_2$ still remains a great challenge. Herein, we developed an ultrahigh efficiency of solid solution $\text{Co}_{0.5}\text{Zn}_{0.5}\text{O}$ (CZO) nanosheets exposed abundant cobalt active sites for PMS activation. The dual Co-Zn sites residing at the CZO surface selectively adsorbed specific O sites of PMS, therefore promoting the generation of $^1\text{O}_2$ with 100% selectivity. The CZO/PMS system showed great adaptability to inorganic ions and pH value with the exclusive $^1\text{O}_2$ species, and the toxicity of antibiotic contaminants was markedly declined after treatment. The CZO nanosheets were attached to fibrous membrane to apply in continuous degradation of organic pollutants with high removal efficiency (95%) over 10 h. This study provides new insights into the development of highly selective catalysts to $^1\text{O}_2$ generation and highlights their potential applications in water purification.

1. Introduction

Antibiotics, such as tetracycline (TC) and ciprofloxacin (CIP), have made outstanding contributions to therapy of bacterial infections in human and poultry. Nevertheless, antibiotics have recently posed a threat to ecological and environmental security [1]. Owing to their antibacterial and ecotoxic properties, antibiotics are difficult to be removed by traditional water treatment methods so that they are considered as a kind of refractory organics [2,3]. Therefore, the treatment of surface water and wastewater, especially, pharmaceutical and medical wastewater with high content of antibiotics, has drawn momentous attention. Peroxymonosulfate (PMS)-based advanced oxidation processes (PMS-AOPs) are regarded as a kind of promising strategy for catalytic degradation of refractory pollutants for water treatment [4]. In the PMS-AOPs, PMS is subsequently converted to certain reactive oxygen species (ROS) including radicals (SO_4^\cdot , $^\cdot\text{OH}$, O_2^\cdot) and non-radicals (singlet oxygen, $^1\text{O}_2$) through catalytic reactions [5,6].

However, ions and natural organic matter (NOM) in water compete with organic contaminants to react with free radicals, which results in reduced efficiency of catalytic pollutant degradation [7]. Among those ROS, $^1\text{O}_2$ is less susceptible to interference from surroundings, including pH, ions, organic and inorganic substances with longer lifetime than other radicals [8]. Therefore, researchers expect to develop catalysts with high selectivity of $^1\text{O}_2$ generation in PMS activation process for the mineralization of organic pollutants.

An explicit mechanism of $^1\text{O}_2$ generation should be explored first to develop a high-selectivity catalyst. In general, superoxide radical (O_2^\cdot) is regarded as crucial precursor for the generation of non-radical products by PMS activation ($\text{O}_2^\cdot + \text{H}_2\text{O} \rightarrow ^1\text{O}_2 + \text{H}_2\text{O}_2 + \text{OH}^\cdot$) [9,10]. However, the disproportionation reaction, Haber-Weiss reaction ($\text{O}_2^\cdot + \text{H}_2\text{O}_2 \rightarrow ^\cdot\text{OH} + \text{OH}^\cdot + \text{O}_2$), inevitably decreases the yield of $^1\text{O}_2$. On the other hand, $^1\text{O}_2$ can be produced by self-decomposed of PMS, but the decomposed rate is awfully slow ($0.2 \text{ M}^{-1} \text{ s}^{-1}$) [11]. Accelerating the decomposition rate is a common strategy to selectively and efficiently generate $^1\text{O}_2$. It is

* Corresponding authors.

E-mail addresses: liuzejin1026@126.com (J. Liu), junli2019@zzu.edu.cn (J. Li).

<https://doi.org/10.1016/j.apcatb.2023.122429>

Received 2 January 2023; Received in revised form 30 January 2023; Accepted 1 February 2023

Available online 2 February 2023

0926-3373/© 2023 Elsevier B.V. All rights reserved.

reported that the generated reactive species and pollutant degradation routes are correlated with the active sites of metal-nonmetallic catalysts [12]. The adsorption of specific O sites of PMS on catalyst can preferentially promote the selectivity of $^1\text{O}_2$ generation [13].

Single-atom catalysts (SACs) are superior in selective and efficient $^1\text{O}_2$ generation than traditional catalysts [14]. Mi et al. [15] proposed that the selectivity for $^1\text{O}_2$ generation was higher than 98% on CoN_{2+2} active sites in Co SACs derived from experimental and theoretical evidence. Nonetheless, the application of SACs in PMS activation has been impeded by the low loadings of active sites [16]. Therefore, rational design of a solid solution catalyst by active metal replacing to increase the active sites with the advantages of SACs is a feasible strategy. Substitutional solid solution is a crystal formed when solute atoms are incorporated into a uniform crystalline matrix, substituting some of the matrix atoms [17]. Solid solution catalysts not only possess high dispersion of active metal, but also have high active metal content, which is conducive to modulate the properties and maximize the effect of catalysts [18]. To achieve successful lattice substitution, the following conditions should be satisfied between the substitutional ion and the substituted ion of matrix materials: (1) approximative ionic radius; (2) similar ionic valence states [19]. In addition, among various metals in preparation of PMS activation catalysts, cobalt-based materials exhibit great activation performance for PMS [20].

Herein, taking a cheap metal oxide ZnO as an example, ultrathin solid solution $\text{Co}_{0.5}\text{Zn}_{0.5}\text{O}$ (CZO) nanosheets with abundant active cobalt sites for PMS activation were designed reasonably. The cobalt atoms are uniformly distributed in zincite lattice as revealed by aberration-corrected high-angle annular dark-field scanning transmission electron microscopy (AC HAADF-STEM) and X-ray absorption spectroscopy (XAS) measurement. The CZO catalyst only needs an extremely short time to achieve high efficiency of TC removal with low dosage in the presence of PMS. In the optimal condition, TC removal efficiency could achieve more than 99% in 5 min by 0.3 g L^{-1} PMS and 0.05 g L^{-1} CZO. Besides, the efficient catalyst CZO was attached on the fibrous membrane to achieve continuous activation of PMS for organic pollutants degradation with removal efficiency over 95% more than 10 h. According to the prediction by ECOSAR software, the toxicity of TC products after treatment by CZO/PMS system was distinctly declined. This study opens an avenue to maximize atomic utilization to achieve efficient PMS activation and high selective $^1\text{O}_2$ production for wastewater treatment.

2. Experimental procedures

2.1. Synthesis of catalysts

The sources of chemicals can be found in Text S1 of the [Supporting Information](#). The CZO catalyst is synthesized by solvothermal method. A certain amount of hexadecyl trimethyl ammonium bromide [CTAB, 200 mg], cobalt nitrate hexahydrate $[\text{Co}(\text{NO}_3)_2 \cdot 6 \text{H}_2\text{O}]$, 600 mg], zinc nitrate hexahydrate $[\text{Zn}(\text{NO}_3)_2 \cdot 6 \text{H}_2\text{O}]$, 300 mg] and potassium nitrate $[\text{KNO}_3]$, 200 mg] were added into 10 mL deionized water in sequence under constant magnetic stirring. The mixture was stirred for 10 min after each addition to ensure the formation of homogeneous solution. Then 30 mL of ethylene glycol was mixed with the as-prepared solution. The mixed solution was maintained at 140°C for 36 h in the Teflon-lined autoclave. After naturally cooling to room temperature, the resulted precipitates were repeatedly washed by deionized water and ethanol to remove soluble impurity ions and dried at 60°C in a vacuum drying chamber. The finally products, purple solid powders, named $\text{Co}_{0.5}\text{Zn}_{0.5}\text{O}$ (abbreviated as CZO). The synthetic procedures of ZnO and Co_3O_4 are shown in Text S2.

2.2. Characterization

The surface morphology and elemental composition were performed

on scanning electron microscopy (SEM, JCM-6000PLUS), transmission electron microscopy (TEM, JEOL JEM 2100 F), atomic force microscope (AFM, AIST-NT), AC HAADF-STEM (FEI Theims Z) and inductively coupled plasma optical emission spectroscopy (ICP-OES, Shmadzu ICPE-9820). The structure of catalyst was analyzed by X-ray diffraction (XRD, Panalytical XPert Pro), X-ray photoelectron spectroscopy (XPS, AXIS Supra) and XAS measurements. The electrochemical properties of as-prepared samples were measured by electrochemical workstation (CHI760E, Chenhua). All electrochemical measurements were performed in a traditional three-electrode configuration using silver/silver chloride electrode (Ag/AgCl) and Pt ring electrode as reference and counter electrode. The specific surface areas and pore distribution of catalysts were calculated by Micromeritics ASAP 2020 applying the Brunauer-Emmett-Teller (BET) equation from the N_2 adsorption-desorption isotherms and the Barrett-Joyal-Halenda (BJH) method.

2.3. Examination of catalytic performance

TC was selected as target contaminants to evaluate the PMS activation performance for organic pollutants removal. Typically, catalyst was dispersed in the glass beaker with 50 mL of pollutant aqueous solution under 400 rpm rotary by magnetic stirring. A certain amount of PMS was added to start the reaction. Without additional explanation, the reaction occurred under the condition of $c_{\text{TC}} = 100 \text{ mg L}^{-1}$, $c_{\text{cat}} = 0.05 \text{ g L}^{-1}$, $c_{\text{PMS}} = 0.3 \text{ g L}^{-1}$. At regular intervals, the sample was drawn out and filtrated by the $0.22 \mu\text{m}$ filter. Then, the concentration of target products was determined by high-performance liquid chromatography (HPLC) and UV-vis spectrometer.

The HPLC was utilized to determine the concentrations of antibiotics with the condition of acetonitrile and water solution with 1% formic acid (25:75 v/v) at 280 nm for TC under 18°C ; 0.025 mol L^{-1} phosphoric acid solution and acetonitrile (87:13 v/v) at 278 nm for CIP under 30°C . The HPLC system (LC 5090, FULL INSTRUMENTS) equipped with a Sunniet C18 column ($4.6 \text{ mm} \times 250 \text{ mm}$, $5 \mu\text{m}$). The concentrations of RhB (554 nm) and MB (664 nm) were determined by UV-vis spectrometer (AQAMATE 8100, Thermo Fisher Scientific).

The pseudo-first-order kinetic model was introduced to fit the reaction kinetics (k) data of TC removal according to Eq. 1:

$$\ln(C/C_0) = -k t \quad (1)$$

Where C and C_0 (mg L^{-1}) represent TC concentrations at time t (min) and before reaction, respectively. k (min^{-1}) is the rate constant fitting with the pseudo-first-order for TC removal.

In order to compare the efficiency of PMS activation with other cobalt-based catalysts, a modified kinetic model, k-value ($\mu\text{mol g}^{-1} \text{min}^{-1}$), was employed, through dividing the reaction rate (k) by the concentration of catalyst followed by multiplying target contaminant concentration according to Eq. 2:

$$k\text{-value} = k / c_{\text{cat}} \times c_{\text{con}} \quad (2)$$

where c_{cat} (g L^{-1}) represents concentration of catalyst, and c_{con} ($\mu\text{mol L}^{-1}$) is the concentration of contaminants.

The flux of membrane J ($\text{L m}^{-2} \text{h}^{-1}$) was averaged and further calculated as the Eq. 3:

$$J = V / (s \times t) \quad (3)$$

Where V (L) represents the volume of the collected solution in t (min) minutes, s represents the effective filtration area of the membrane.

2.4. Measurement and computational details

The details of XAS measurement and computational methods can be found in Text S3-S4 of [supporting information](#), respectively.

3. Results and discussion

3.1. Synthesis and structural analysis of CZO

The schematic diagram in Fig. 1a describes the one-step solvothermal synthesis method of CZO catalysts. The morphological and microstructural features of CZO are displayed in electron microscopy images. Obviously, sharp and ultrathin architecture of two-dimensional (2D) nanosheets can be observed in HAADF-STEM pattern (Fig. 1b-c), similarly in the SEM (Fig. S1) and TEM (Fig. S2) patterns. The element distribution of the CZO catalyst was exhibited by the energy dispersive spectroscopy (EDS) in Fig. 1d, indicating that each element was greatly dispersed and the Co: Zn mass was determined as 21.5: 26.8 on the surface in Fig. S3. The AFM image in Fig. 1e with homogeneous color revealed their average 3.5 nm thickness of the ultrathin nanosheets. The enlarged image of the STEM in Fig. 1f displayed the microscopic

arrangement of uniformly hexagonal atoms. To further identify the atomic composition and arrangement of the Co and Zn atoms, we measured the atomic separation along the green line in Fig. 1g. Interestingly, the intensity profile transformed from STEM images exhibited a periodic oscillation change of distance between the connection-two-atom, indicating a highly monodispersed and uniform distribution of Co atoms, which replaced Zn atoms in the ZnO lattice [21]. The BET surface area (Fig. S4) of the CZO catalyst is $63.77 \text{ m}^2 \text{ g}^{-1}$, which is 14.5 times bigger than that of ZnO ($4.13 \text{ m}^2 \text{ g}^{-1}$). The nanosheets CZO catalyst exhibits larger specific surface area than the as-prepared ZnO, leading to preferable contact of the active sites. ICP results were consistent with EDS analysis results, implying that the as-prepared nanosheets catalyst with a Co: Zn molar ratio of 1: 1 approximately, labeled as $\text{Co}_{0.5}\text{Zn}_{0.5}\text{O}$ (CZO).

XRD patterns were acquired as shown in Fig. S5, which were in consistent with the standard card of zinc oxide (ZnO) without extra

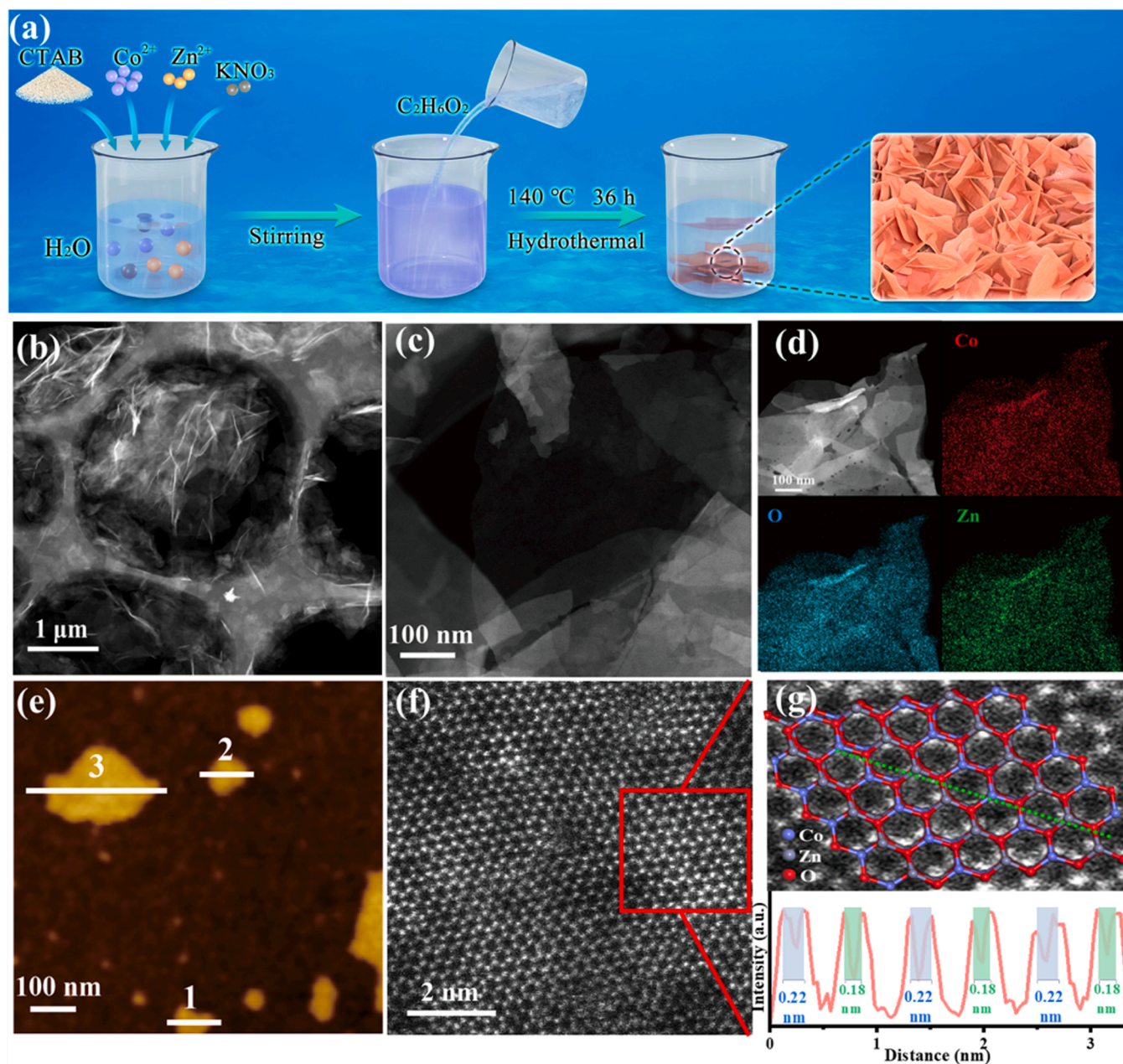


Fig. 1. (a) Schematic illustration of the synthesis pathways of CZO. (b-c) AC HAADF-STEM images. (d) EDS pattern. (e) AFM image of CZO nanosheets. (f) AC HAADF-STEM images and (g) the corresponding height profile along the green line.

peaks. It was proved that after Co substituted Zn site in ZnO crystal lattice, the structure of zincite was preserved, which further proved that Co atoms had been successfully introduced into ZnO as the form of solid solution. The surface elemental composition and the chemical states of CZO were further characterized by X-ray photoelectron spectra (XPS). The XPS survey spectra of as-prepared catalysts exhibited in Fig. S6, which is the evidence of the presence of Co, Zn and O elements without other impurities (C 1 s peak was used as the reference for calibration). In detail, two distinctive peaks of Zn 2p located at 1045.9 and 1022.0 eV can be identified as Zn 2p_{1/2} and Zn 3/2 orbital, respectively [22]. The binding energy of Zn slightly shifted to higher orientation in comparison to the Zn 2p (1044.3 and 1021.2 eV) in the as-prepared ZnO, suggesting that Zn lost some electrons after introduction of Co. Curves fitting of the Co 2p XPS spectra in Fig. 2a showed three peaks at 780.9, 782.2, 786.9 eV corresponded to Co³⁺, Co²⁺ and satellite peak in Co 2p_{3/2} area respectively, while Co 2p_{1/2} was assigned the three peaks at 796.3, 797.5, 802.7 eV, similarly. Specifically, the ratio of Co²⁺ peak area (75.8%) among the gross cobalt indicated that +2 valence is majority state of the superficial cobalt in catalyst. From the result of EPR, there is oxygen vacancy existing in ZnO as shown in Fig. S7.

To further confirm the occupation position of Co atoms in CZO solid solution, XAS measurements were carried out. From the Fig. 2b, the Co K-edge XANES spectra showed the absorption edge position was quite close to Co²⁺ in CoO, indicating the Co²⁺ in CZO samples. According to

the EXAFS analysis (Fig. 2c-d, Table S1), there is no peak related to Co-Co (2.18 Å) in the CZO catalyst, which further excluded the presence of metal Co or cobalt nanocluster in the samples. The peak of CZO curved by K-edge EXAFS at 1.60 Å can associate with Co-O and the peak at 2.73 Å results from Co-Co/Zn [23]. Through theoretical calculation, it is concluded that the Co-Co bond in CZO is unstable, so it is speculated as Co-Zn bond at 2.73 Å. All the above results lead us to conclude that CZO was successfully obtained, in which Co atoms partly substitute the Zn sites. The structure of CZO can be portrayed as the “sixfold cavities” as shown in Fig. 2e. The WT-EXAFS of CZO in Fig. 2f-i exhibits exhibited different distribution from Co foil and Co oxides, further confirmed its special structure.

3.2. Performance of ZnO and CZO for activating PMS

To evaluate the catalytic performance of CZO, we chose TC as targeted pollutant to evaluate the catalytic efficiency of PMS activity. As shown in Fig. 3a, the degradation rate of CZO/PMS system for TC was much higher than other systems. The degradation rates (k) with CZO/PMS, ZnO/PMS and CZO/H₂O₂ were 1.16, 0.049 and 0.013 min⁻¹, respectively (Fig. 3b). In addition, the degradation rate (k) with CZO/PMS was 16.5 times higher than the sum of ZnO/PMS and Co₃O₄/PMS (0.022 min⁻¹) in Fig. S8. Besides, the degradation rate with CZO/PMS system was approximately 41 times than that PMS merely (0.02851 min⁻¹

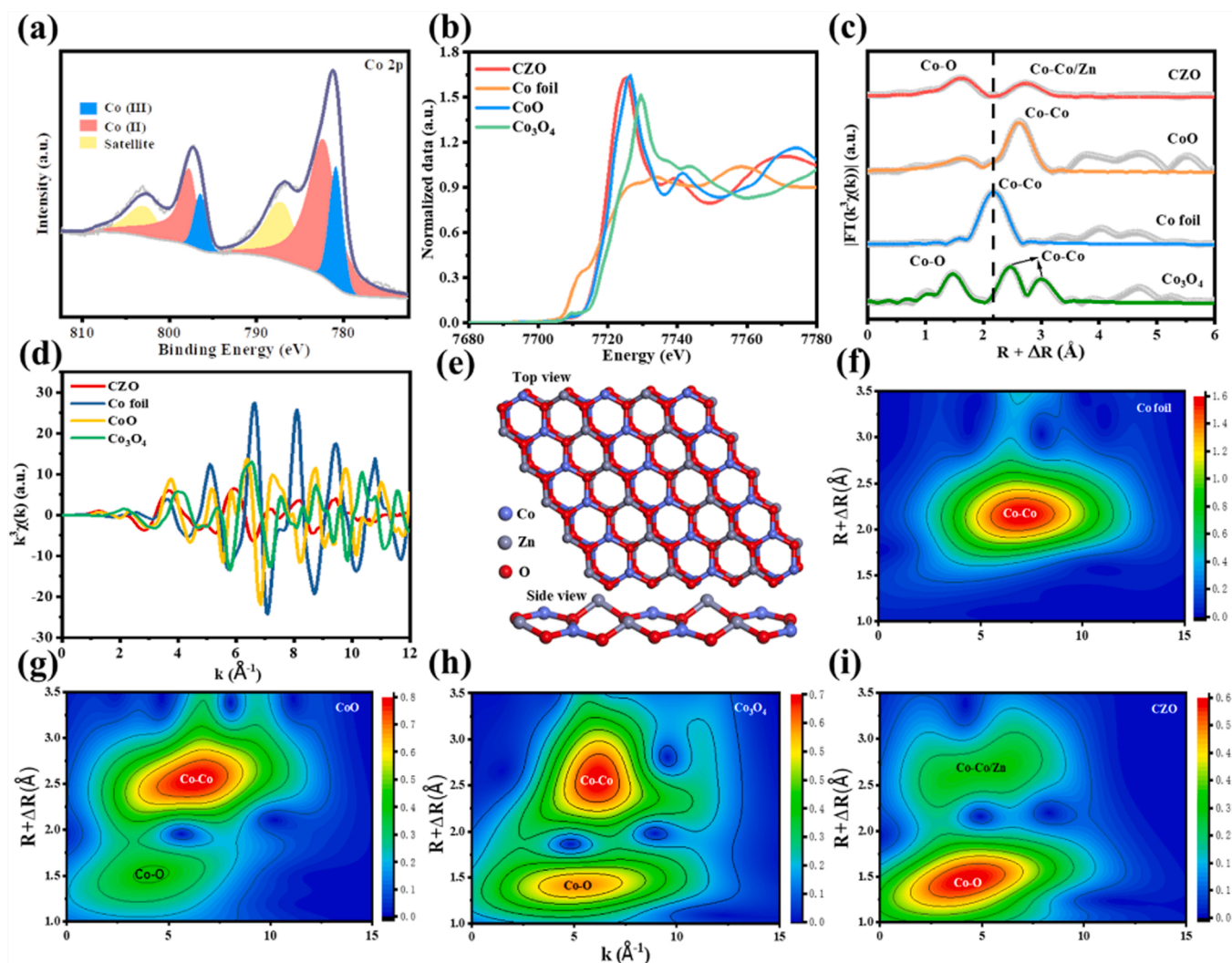


Fig. 2. (a) XPS spectra of CZO: Co 2p spectra. (b) Normalized Co K-edge XANES, (c) Fourier transform EXAFS spectra and (d) k^3 -weight analysis of CZO. (e) The structural model of CZO. Wavelet transform analysis of (f) Co foil, (g) CoO, (h) Co₃O₄ and (i) CZO.

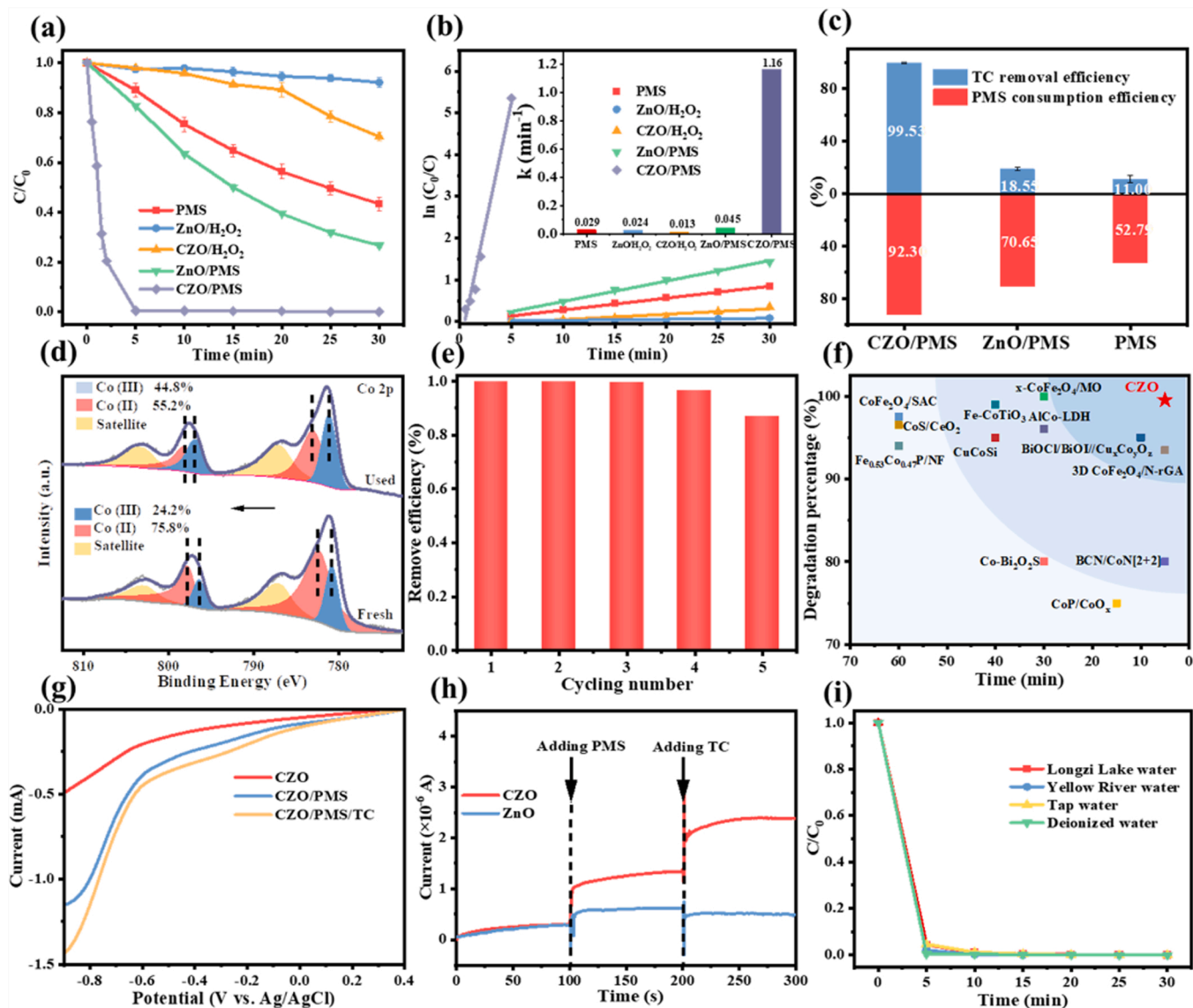


Fig. 3. (a) The TC degradation activity curves in different systems with (b) the corresponding kinetic curves. (c) TC degradation ratio and PMS consumption ratio in CZO/PMS system for 5 min (d) The XPS spectrum of Co 2p for CZO before and after reaction. (e) Cyclical performance of CZO powders for TC degradation. (f) Summary and comparison of TC degradation percentage and time for CZO and other cobalt-based catalysts. (g) The LSV curves and (h) chronoamperometry curves of ZnO and CZO under different conditions. (i) Catalytic performance of CZO in natural water samples.

¹). The TC removal efficiency surprisingly reached 99.53% in only 5 min in the presence of PMS and CZO, exhibiting excellent oxidation ability of CZO/PMS system. The optimized catalyst shows much better PMS activation ability than the as-prepared ZnO and Co_3O_4 , and greatly enhances the removal ability of TC, despite the dosage of catalyst is just 0.05 g L^{-1} which is one fifth of the PMS dosage.

TC removal efficiency and PMS utilization efficiency within 5 min were provided in Fig. 3c, certifying the outstanding efficiency for PMS activation in a short time over CZO catalyst. The efficiency of PMS consumption in CZO/PMS system is also higher than ZnO/PMS system and PMS merely, which means the presence of CZO accelerates the decomposition of PMS and promotes electron transfer. PMS was decomposed rapidly (92.30%) and TC was degraded promptly (99.53%) in a short time (5 min). In the ZnO/PMS system, 70.65% of PMS was consumed within 5 min, whereas the TC removal efficiency was only 18.55% indicating the PMS was not utilized effectively. The excellent performance of CZO/PMS system for TC degradation can be seen clearly from the HPLC results in Fig. S9. The peaks representing TC with appearing time near 3.9 min (test time), which almost disappeared after

5 min reaction, indicating that TC was degraded to a great extent.

The XPS spectra of CZO fresh and used were compared in Fig. S10. The position of the peaks hardly shifted, indicating the stability of the catalysts. The XPS results also revealed the valence state changes about cobalt element. As shown in Fig. 3d, Co^{3+} takes up a small fraction (24.2%) of the total cobalt in fresh catalyst, while after reaction, the number significantly escalates to 44.8%. The consequence implied that Co^{2+} took part in the activation of PMS and a part of Co^{2+} was oxidized to Co^{3+} during the reaction [24]. The reusability and stability of CZO powders were investigated and the results were presented in Fig. 3e. The TC removal efficiency within 30 min in five cycle runs were 99.9%, 99.8%, 99.6%, 96.5% and 86.8%, respectively. The deactivation can be attribute to the mass loss of catalyst, indicating the excellent properties for potential applications. In addition, the TEM images (Fig. S11) of CZO after reaction had no obvious change in the nanosheets, indicated the favorable stability of CZO.

Furthermore, considering the amount of catalyst and the concentration of pollutants, a modified kinetic (k-value) was compared with various cobalt-based catalyst systems (Table S2). The k-value of CZO/

PMS system is as high as $1.348 \mu\text{mol g}^{-1} \text{min}^{-1}$, which is 1.7–224.7 times of that of other reported cobalt-based contaminant removal systems. Then, we compared the TC removal performance of CZO with the recently reported cobalt-based catalysts intuitively in Fig. 3 f (the literatures are shown in Table S3). It is distinctly manifested the excellent performance of CZO/PMS system to degrade TC and displayed the outstanding activity of CZO catalysts among the latest reported catalysts and the promising future of application in water treatment [25].

The electrochemical evaluation was carried out to further illuminate the catalytic performance and explore the catalytic mechanism of CZO/PMS system. The EIS Nyquist plots (Fig. S12) manifested that CZO has a smaller resistance and higher conductivity in electricity than ZnO, which leads to a faster interface electron transfer. The resistance of CZO further decreased in the presence of PMS. This results convincingly verified that more and faster electron transfer accelerated the activation of PMS by CZO. In addition, linear sweep voltammetry (LSV) analysis (Fig. 3 g) and chronoamperometry curve (Fig. 3 h) provide the proof that the current for CZO electrode increased conspicuously with the presence of PMS. According to the electrochemical analysis results, the proof of electron transfer was provided that the current for CZO electrode increased with the presence of PMS.

In addition, several natural water samples (Yellow River water, Longzi Lake water, tap water) were employed to evaluate the effect to CZO/PMS system with natural backgrounds on the degradation of TC. The result in Fig. 3 i demonstrated excellent adaptability of CZO/PMS system to adapt general circumstances of wastewater.

3.3. Combination of CZO/PMS system with membrane technology

However, we found traditional powder catalysts are difficult to recover and recycle [26], therefore, we tried to integrate the nanosheets CZO catalysts with the fibrous membrane. It is apparent that the as-prepared CZO fibrous membrane can be convenient for recycle and is potentially adapted to application on practical wastewater treatment with high concentration of organic pollutants [27]. Attaching PMS-activation catalysts on the membrane for pollutants removal has been proposed as an attractive approach for water treatment, but its practical application was impeded by the high demands of catalyst activity due to the short contact time of wastewater with membrane surface [28]. Given the excellent activity of CZO, the nanosheets catalysts were further applied in the membrane technology. As shown in Fig. 4a, the pristine fibrous membrane substrate was made up of crisscrossed filaments [29]. The CZO fibrous membrane (the efficient diameter is 65 mm) was fabricated by simply vacuum-assisted filtering CZO suspensions via fibrous membrane substrate as shown in Fig. S13. As shown in Fig. 4b, the nanosheets CZO catalysts were embedded in the gap of filaments and randomly distributed on the fiber membrane. The membrane was then clamped to a rubber ring and support plate with small holes for continuous water treatment (Fig. 4c-d). To better observation, we select RhB dye as target pollutant to evaluate the continuous degradation capacity of CZO fibrous membrane/PMS system. Water flux is an important property of membrane [30,31]. The flux remained nearly unchanged with ($130.6509 \text{ L m}^{-2} \text{ h}^{-1}$) or without ($129.8935 \text{ L m}^{-2} \text{ h}^{-1}$) CZO catalysts on the membrane (Fig. 4e). These indicated that CZO

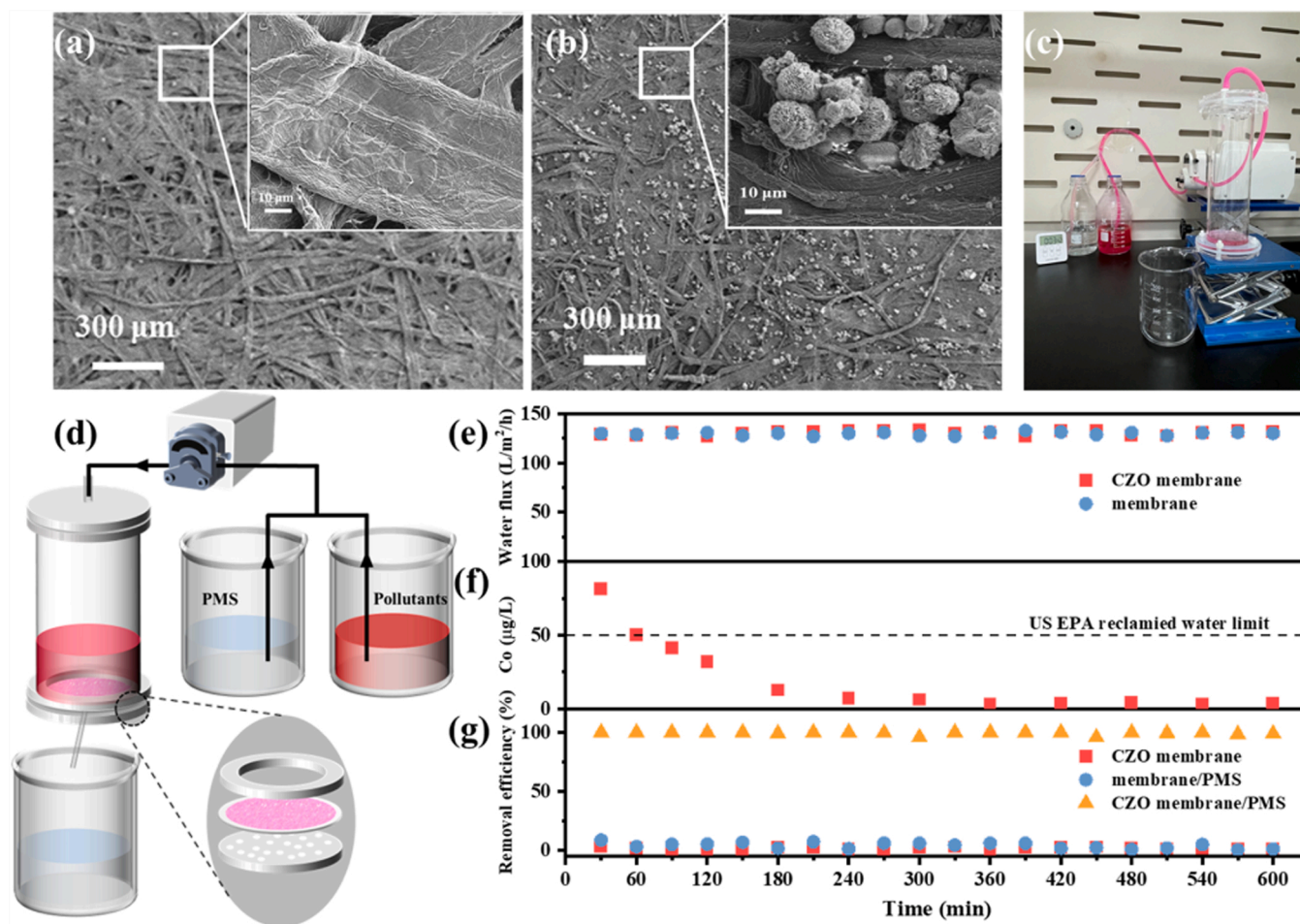


Fig. 4. SEM images of (a) pristine fibrous membrane and (b) CZO fibrous membrane. (c) Photograph of continuous experiment device. (d) Schematic diagram of continuous water treatment plant. (e) The water performance of different fibrous membranes. (f) The Co concentration detected in the treated water. (g) The pollutants degradation performance of different fibrous membranes.

fibrous membrane/PMS system were ultrahigh efficient to degrade pollutants for a short time. In the continuous water treatment system, the Co ion concentration was detected, which maintained below the US Environmental Protection Agency ($50 \mu\text{g L}^{-1}$) after an hour (Fig. 4f). As shown in Fig. 4g, the pristine fibrous membrane had a small contribution to the decontamination of pollutants. Interestingly, CZO fibrous membrane/PMS system under down-flow operating mode achieved stable and efficient removal of organic pollutant with a removal efficiency higher than 95% over 10 h.

3.4. Identification of active species

In order to give insights into the reaction mechanism in the PMS system, the ROS in the reaction process was identified by quenching experiment. Quenching experiments were carried out to identify the ROS taking effect in the CZO/PMS reaction system using different scavengers in Fig. 5a: p-benzoquinone (p-BQ) for $\text{O}_2^{\bullet-}$; Methanol (Me-OH) for $\text{SO}_4^{\bullet-}$ and $\bullet\text{OH}$; furfuryl alcohol (FFA) for $^1\text{O}_2$. There was no markedly inhibitory effect on the degradation of TC when the scavengers of p-BQ, Me-OH were introduced into the reaction system, indicating the absence of $\text{O}_2^{\bullet-}$, $\text{SO}_4^{\bullet-}$ and $\bullet\text{OH}$. When FFA was added, the degradation rate of TC was clearly depressed and the rate ulteriorly descend with the increasing FFA dosage in Fig. S14. The results confirmed that there is no other than $^1\text{O}_2$ as the active species in CZO/PMS system. In addition, the degradation rate remained unchanged in the presence of p-BQ, which

confirms that the active species ($^1\text{O}_2$) is not derived from $\text{O}_2^{\bullet-}$ in CZO/PMS system. Furthermore, in order to eliminate the influence of dissolved O_2 or O_2 in the air, a comparison experiment was employed under a N_2/O_2 atmosphere [32] in Fig. S15. The results revealed that the catalytic performance does not obviously decrease, confirming that $^1\text{O}_2$ is originated from the decomposition of PMS.

The validity of above conclusion can also be proved by EPR technology. DMPO was conducted to capture free radicals such as $\bullet\text{OH}$, $\text{SO}_4^{\bullet-}$ and $\text{O}_2^{\bullet-}$. TEMP was conducted to capture the non-radical ($^1\text{O}_2$). As shown in Fig. S16a, no enhanced EPR signal of $\bullet\text{OH}$ (intensities of 1:2:2:1) or $\text{SO}_4^{\bullet-}$ (intensities of 1:2:1:2:1:2:1) could be detected after addition of CZO in the PMS aqueous solution, indicating the absence of $\text{SO}_4^{\bullet-}$ and $\bullet\text{OH}$ [33,34]. In addition, no characteristic signal can be observed for $\text{DMPO-O}_2^{\bullet-}$ (six peaks in the presence of methanol, Fig. S16b), suggesting that $^1\text{O}_2$ is not generated via $\text{O}_2^{\bullet-}$ intermediate. Relatively, three characteristic peaks (intensities of 1:1:1) of $\text{TEMP-}^1\text{O}_2$ were significantly detected in CZO/PMS system in Fig. 5b [35]. The above results confirmed that $^1\text{O}_2$ is the exclusive active species in CZO/PMS system while avoiding the Haber-Weiss competitive reaction [13]. The generation of $^1\text{O}_2$ accounted for 100% proportion of reactive species.

3.5. Performance of CZO for TC degradation

The effect of initial pH at the range of 3–11 was present at Fig. 5c,

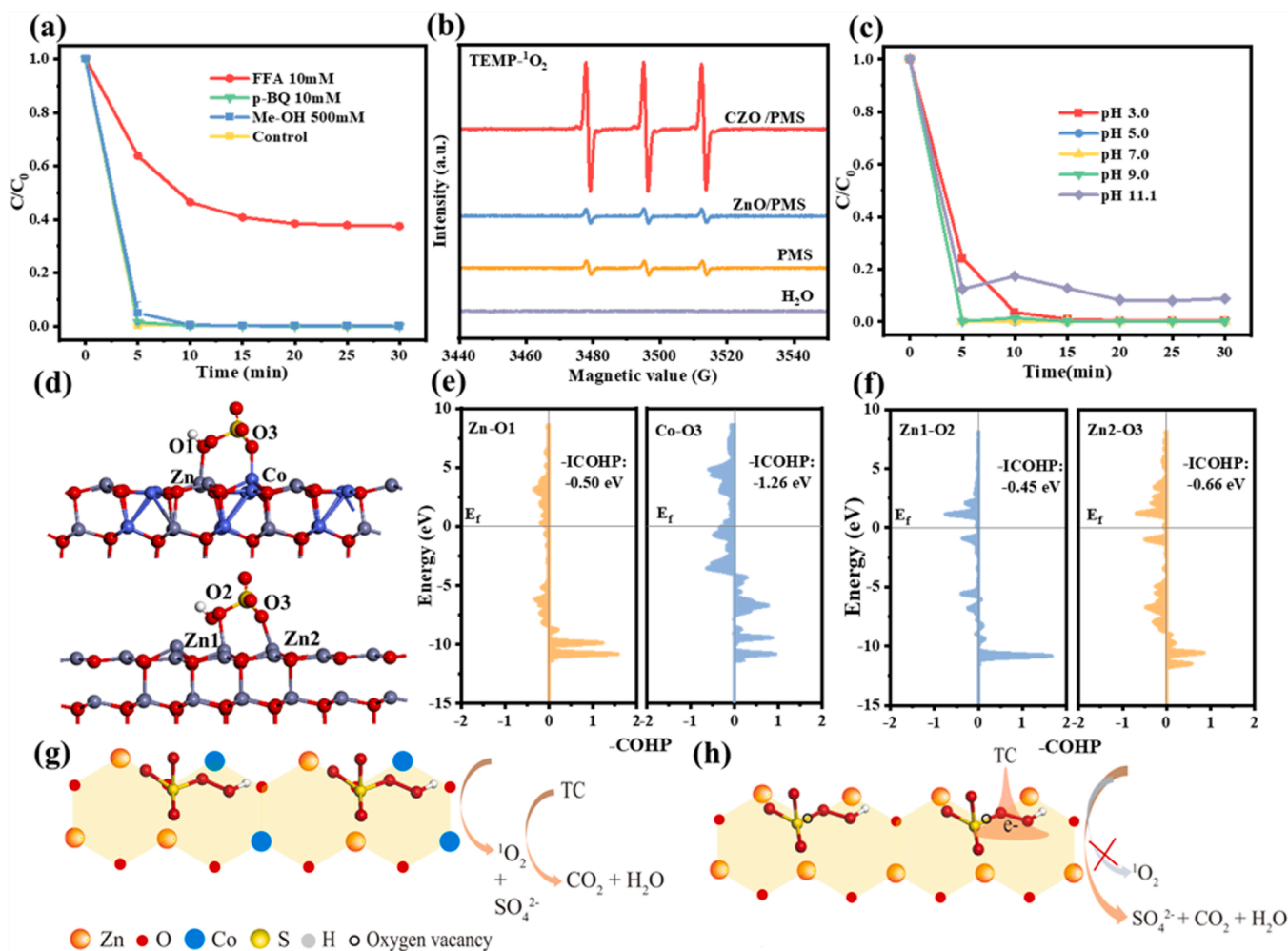


Fig. 5. (a) TC degradation performance of CZO/PMS system with different kind of ROS scavengers. (b) EPR signals of $\text{TEMP-}^1\text{O}_2$ for different systems. (c) Effect of original solution pH for TC degradation. (d) The optimal PMS adsorption model on CZO and ZnO. COHP for the metal-O of absorbed PMS on the (e) CZO and (f) ZnO. Schematic diagram of PMS activation on the (g) CZO and (h) ZnO.

demonstrating that $^1\text{O}_2$ active species have outstanding TC removal performance in a wide pH range. In a relatively mild environment, the oxidation efficiency of TC is able to reach more than 90% in 30 min.

The influence of oxidant concentration and catalyst dosage on degradation of target pollutant were evaluated because they were potential influence factors to affect catalytic performance of TC removal. As shown in Fig. S17a, an increased degradation rate was observed when the catalyst dosage increased from 0.01 to 0.05 g L⁻¹, while it remained no further improve when the dosage increased from 0.05 to 0.1 g L⁻¹. Therefore, we select 0.05 g L⁻¹ as the optimal dosage of catalyst. The similar phenomenon occurred in the experiment dependent on the PMS concentration (Fig. S17b). As a result, we choose the catalyst dosage and PMS concentration of 0.05 and 0.3 g L⁻¹, respectively, as the optimum condition for further study.

The realistic wastewater is accompanied by multiple inorganic anions and cations in general [36]. Fig. S18 showed the effects of ubiquitous anions (Cl^- , NO_3^- , SO_4^{2-} , CO_3^{2-}), cations (K^+ , Ca^{2+} , Na^+ , Mg^{2+}) on the removal of TC by oxidation of CZO/PMS system. As the experiment results displayed, the degradation of TC with the existence of CO_3^{2-} dropped down to 84.49% after reaction for 5 min, from the controlling condition of 99.86%. Except for CO_3^{2-} , the curves of the TC degradation with and without the additive anions (Cl^- , NO_3^- and SO_4^{2-}) almost overlap with the other, suggesting that the influence of the inorganic anions is so subtle that it can be nearly ignored. A similar phenomenon was observed in cations influence experiment. After the common cations (K^+ , Ca^{2+} , Na^+ , Mg^{2+}) adding to the initial solution, the degradation curves were hardly deviation, implying the strong resistance to aqueous circumstances of CZO/PMS system [37].

In addition, the degradation universality toward different kind of persistent organic pollutants was evaluated in Fig. S19. All of these pollutants, including dyes (RhB, MB) and antibiotics (CIP, TC) were degraded by CZO/PMS system, with removal efficiencies better than 75% in 30 min. All of these results demonstrate the excellent adaptability of CZO for PMS activation to decontamination of organic pollutants in general wastewater.

In order to evaluate the effect of physical adsorption of pollutants by catalysts, the removal efficiency of TC by the catalyst without the addition of PMS was also measured in Fig. S20. Adsorption of CZO contributed only a small portion for target pollutant removal (< 9.5%), while the remove of the mere ZnO for TC is nearly negligible, suggesting that the present of CZO significantly improves the activity of PMS decomposition for the degradation of organic contaminants.

3.6. $^1\text{O}_2$ generation analysis in theory

DFT calculation was used to determinate the mechanism of synergic catalysis between Co and Zn sites for $^1\text{O}_2$ generation. Based on characterization and structural optimization, we adopted the proposed catalyst structure and PMS adsorption model. In the optimal adsorption structure, the PMS is bonded with different metal sites on CZO (Zn-O1, Co-O3) and ZnO (Zn1-O2, Zn2-O3) in Fig. 5d. Crystal orbital Hamilton population (COHP) analysis was employed to investigate the chemical bonding that accompany the variation of PMS adsorption. The absolute value of integrated COHP (ICOHP) is positively correlated to the bonding strength and stability. The results show that the bonding stability on CZO ($|\text{ICOHP}|_{\text{Zn-O1}} = 0.50$ eV, $|\text{ICOHP}|_{\text{Co-O3}} = 1.26$ eV, Fig. 5e) is significantly higher than ZnO ($|\text{ICOHP}|_{\text{Zn-O1}} = 0.45$ eV, $|\text{ICOHP}|_{\text{Co-O3}} = 0.66$ eV, Fig. 5f), which indicated that CZO is more conducive to PMS adsorption and activation reaction. Based on the Bader charge analysis in Fig. S21a, electrons accumulate on O1 and O2 which transferred from Co and S atom and hence weaken the O-O bond, which facilitates the O-O bond cleavage to form the $^*\text{HSO}_4\text{-O}$ intermediates on CZO catalyst. By contrast, in Fig. S21b the high local charge accumulation on the O2 is more easily broken to generate unnecessary -OOH intermediates, followed by O-O bond cleavage to form the $^*\text{HSO}_4\text{-O}$ intermediates on ZnO catalyst. Inspired by the above advantages, CZO catalyst is reasonable to

selectively generate $^1\text{O}_2$ in theory in Fig. 5g. Contrastingly, the promotion of ZnO oxidation of organics by PMS may be attributed to the non-radical path caused by its oxygen vacancy as shown in Fig. 5h [38].

3.7. Intermediate analysis of TC degradation and toxicity evaluation

The main intermediates of degradation process were detected by LC-MS technique (Fig. S22-S23). During the catalytic reaction, $^1\text{O}_2$ is the dominant active species, which attacks and breaks TC to smaller organics. According to the testing result, we proposed two possible degradation pathways of TC in CZO/PMS system (Fig. S24). Hydroxylation occurred in the Pathway I followed by deamidation process, due to the generation of p1 ($m/z = 461$) and p2 ($m/z = 378$). Pathway II can divide to three stages. First of all, the TC molecule was decomposed into p3 ($m/z = 432$) and p4 ($m/z = 415$) by demethylation and dehydroxylation. Then the products were further attacked by the active species ($^1\text{O}_2$), so that the benzene rings get cleavage, and the products were transformed to p5 ($m/z = 338$), p6 ($m/z = 299$). Subsequently, the pathway I and Pathway II converged at a suite of lower molecular weight organics ($m/z < 200$). Through a series of oxidation reaction, we got p7 ($m/z = 164$), p8 ($m/z = 149$), p9 ($m/z = 74$) [39,40] and other smaller molecular matter.

In addition, the ecological structure activity relationship (ECOSAR) model class program was utilized to further evaluate and predict the ecotoxicity of TC and process products for acute (short term) and chronic (long term) towards fish, daphnid and green algae (Table S4). According to the Globally Harmonized System of Classification and Labeling of Chemicals, the toxicity can be classified into four toxicity levels, very toxic, toxic, harmful and not harmful (Table S5). The trend of toxicity is described in Fig. S25 through the reaction of TC degradation. Although several process products (p1, p2, p4, p5, p6, p7) exhibit similar to or greater than that of TC, the final products (p8, p9) are classified into not harmful level both long-term and short-term towards fish, daphnid and green algae, which was more eco-friendly than the original TC molecules. Therefore, the toxicity of TC is markedly declined after treatment by CZO/PMS system.

3.8. Mechanism of PMS activation

DFT calculations were employed to investigate the role of Co atoms in CZO for PMS activation. The density of states (DOS, in Fig. 6a-b) was given with and without the introduction of Co element. The DOS intensity at Fermi level is non-zero, indicating a metallic property, which is conducive of the electron transfer in the as-prepared CZO catalyst [41]. Specifically, the overlapping of d-orbitals of Co and TDOS at Fermi level reveals the dominant promotion of cobalt introduction to the ability of electron transfer [42]. It's worth noting that the DOS intensity of CZO is extremely higher than that of ZnO owing to its high electron density around. The large spin density is more favorably for the chemical interaction with PMS. The formation of electron depletion centers (metal sites on catalyst) and electron accumulation centers (O atoms on PMS) were conducted by the charge difference analysis, indicating tendency of the electron transfer from metal-centers to PMS in Fig. S26.

To further unveil the reaction pathway and activation mechanisms to $^1\text{O}_2$ production, the Gibbs free energy (ΔG) of activation step for PMS on the surface of CZO and the corresponding optimized structures of intermediates are calculated in Fig. 6c-d. Apparently, the evolution of $^1\text{O}_2$ by the self-decomposition of PMS over CZO is exergonic and spontaneous ($\Delta G = -10.38$ eV), which is more conducive than that over ZnO ($\Delta G = -9.42$ eV, Fig. S27). In this process, the Co-Zn sites selectively adsorbed the special O site of PMS played a key role to generation of $^1\text{O}_2$ with 100% selectivity over CZO.

4. Conclusion

In this work, ultrathin solid solution CZO nanosheets were

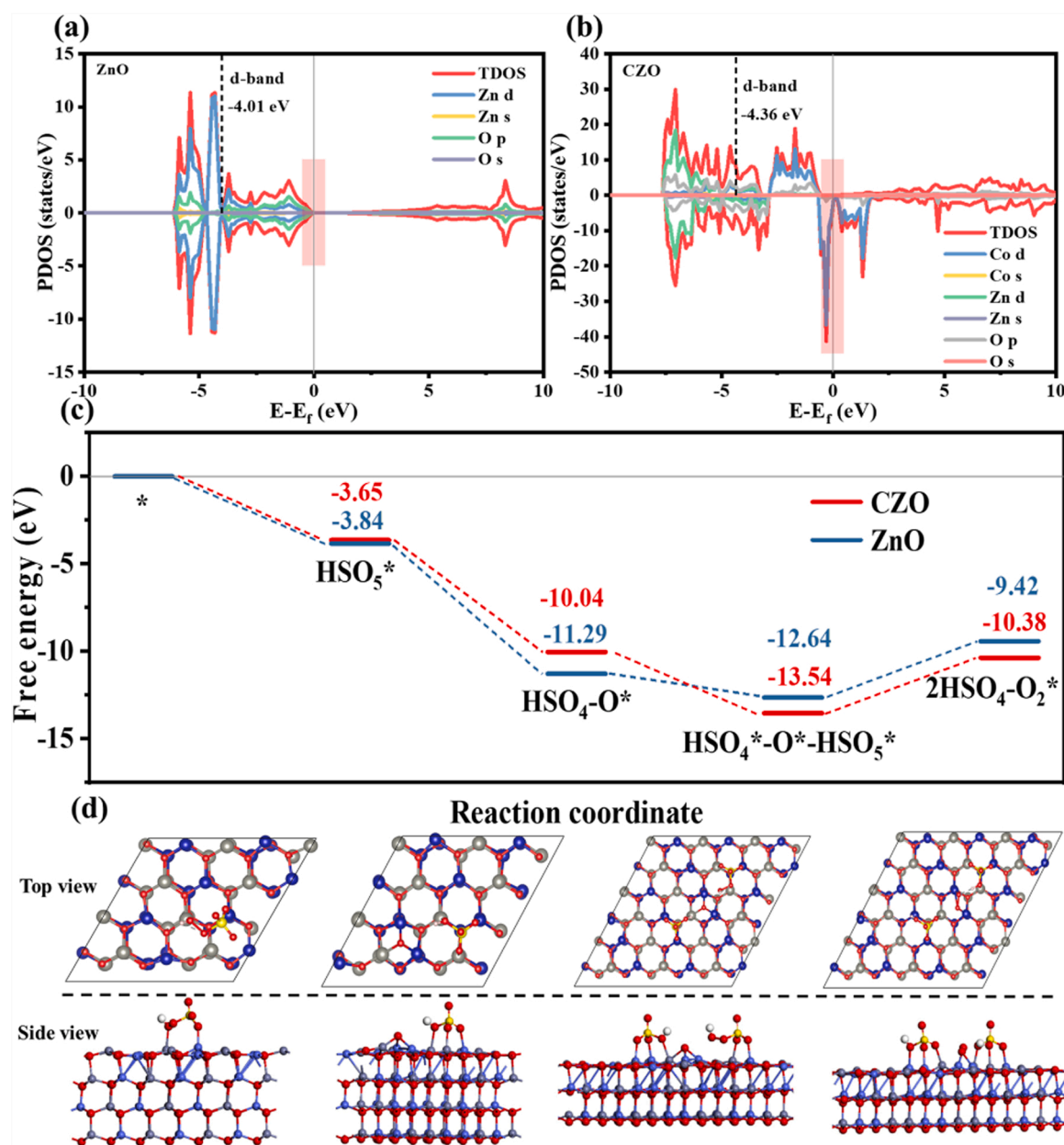


Fig. 6. PDOS of (a) ZnO and (b) CZO. (c) Gibbs free energy of PMS activation to $^1\text{O}_2$ generation on CZO. (d) Optimized geometric structure of PMS on CZO model.

successfully synthesized to activate PMS for pollutant degradation with high efficiency, selectivity, stability, and environmental friendliness. The results of experiment and DFT showed the crucial role of the dual Co-Zn sites for enhanced generation of $^1\text{O}_2$ with 100% selectivity. The introduction of Co promotes the transfer of electrons from catalysts to PMS, thus accelerating the activation of PMS. In CZO/PMS system, TC removal ratio could achieve more than 99% in 5 min and the $^1\text{O}_2$ was generated with 100% selectivity as the sole reactive species. Furthermore, the combination of efficient CZO catalysts with membrane technology facilitates practical application of CZO to wastewater treatment continuously. This research not only provides a new thought for designing high-efficient catalyst with dual metal sites, but also gives deep insights to the non-radical pathway of PMS activation for the practical application.

CRediT authorship contribution statement

J. Li constructed and planned the whole project. X. Zhang performed

the synthesis, characterization, and photocatalysis. J. Liu, H. Zhang and Z. Wan performed the analyses of ESR, TEM, XAFS and DFT results. X. Zhang. writing—original draft, J. Li. writing—review and editing.

Declaration of Competing Interest

The authors declare that they have no known competing financial interests or personal relationships that could have appeared to influence the work reported in this paper.

Data availability

Data will be made available on request.

Acknowledgements

This work was financially supported by National Natural Science Foundation of China (No. 21906184), Outstanding Talent Research

Fund of Zhengzhou University, China Postdoctoral Science Foundation (No. 2020TQ0277, 2020M682328), China Scholarship Council (No. 202108410356), Science and Technology Project of Henan Province (No. 202102310274) and Postdoctoral Science Foundation of Henan province (No. 202002010).

Appendix A. Supporting information

Supplementary data associated with this article can be found in the online version at doi:10.1016/j.apcatb.2023.122429.

References

- [1] B. Gao, Y. Pan, H. Yang, Enhanced photo-Fenton degradation of fluoroquinolones in water assisted by a 3D composite sponge complexed with a S-scheme $\text{MoS}_2/\text{Bi}_2\text{S}_3/\text{BiVO}_4$ ternary photocatalyst, *Appl. Catal. B: Environ.* 315 (2022), 121580.
- [2] Q. Ma, R. Song, F. Ren, H. Wang, W. Gao, Z. Li, C. Li, Photoelectrocatalytic degradation of refractory pollutants over WO_3/W network photoelectrode with heterophase junction for enhancing mass transportation and charge separation, *Appl. Catal. B: Environ.* 309 (2022), 121292.
- [3] K. Wang, X. Shao, K. Zhang, J. Wang, X. Wu, H. Wang, OD/3D $\text{Bi}_3\text{TaO}_7/\text{ZnIn}_2\text{S}_4$ heterojunction photocatalyst towards degradation of antibiotics coupled with simultaneous H_2 evolution: In situ irradiated XPS investigation and S-scheme mechanism insight, *Appl. Surf. Sci.* 596 (2022), 153444.
- [4] L. Wang, H. Xu, N. Jiang, Z. Wang, J. Jiang, T. Zhang, Trace cupric species triggered decomposition of peroxymonosulfate and degradation of organic pollutants: Cu(III) being the primary and selective intermediate oxidant, *Environ. Sci. Technol.* 54 (2020) 4686–4694.
- [5] X. Zhou, M. Luo, C. Xie, H. Wang, J. Wang, Z. Chen, J. Xiao, Z. Chen, Tunable S doping from Co_3O_4 to Co_9S_8 for peroxymonosulfate activation: Distinguished radical/nonradical species and generation pathways, *Appl. Catal. B: Environ.* 282 (2021), 119605.
- [6] S. Ma, D. Yang, Y. Guan, Y. Yang, Y. Zhu, Y. Zhang, J. Wu, L. Sheng, L. Liu, T. Yao, Maximally exploiting active sites on Yolk@shell nanoreactor: Nearly 100% PMS activation efficiency and outstanding performance over full pH range in Fenton-like reaction, *Appl. Catal. B: Environ.* 316 (2022), 121594.
- [7] Z. Gao, J. Liu, C. Skurie, Y. Zhu, Y.S. Jun, Photochemical reactions of dissolved organic matter and bromide ions facilitate abiotic formation of manganese oxide solids, *Water Res.* 222 (2022), 118831.
- [8] T. Liu, D. Zhang, K. Yin, C. Yang, S. Luo, J.C. Crittenden, Degradation of thiacloprid via unactivated peroxymonosulfate: The overlooked singlet oxygen oxidation, *Chem. Eng. J.* 388 (2020), 124264.
- [9] J. Fan, H. Qin, S. Jiang, Mn-doped g- C_3N_4 composite to activate peroxymonosulfate for acetaminophen degradation: The role of superoxide anion and singlet oxygen, *Chem. Eng. J.* 359 (2019) 723–732.
- [10] B.L.A. Schurmann, D. Mollenhauer, J. Janek, D. Schroder, Singlet oxygen in electrochemical cells: A critical review of literature and theory, *Chem. Rev.* 121 (2021) 12445–12464.
- [11] H. Yang, J. Zhou, E. Yang, H. Li, S. Wu, W. Yang, H. Wang, Magnetic Fe_3O_4 -N-doped carbon sphere composite for tetracycline degradation by enhancing catalytic activity for peroxymonosulfate: A dominant non-radical mechanism, *Chemosphere* 263 (2021), 128011.
- [12] N. Li, R. Li, X. Duan, B. Yan, W. Liu, Z. Cheng, G. Chen, L. Hou, S. Wang, Correlation of active sites to generated reactive species and degradation routes of organics in peroxymonosulfate activation by Co-loaded carbon, *Environ. Sci. Technol.* 55 (2021) 16163–16174.
- [13] L. Zhang, X. Jiang, Z. Zhong, L. Tian, Q. Sun, Y. Cui, X. Lu, J. Zou, S. Luo, Carbon nitride supported high-loading Fe single-atom catalyst for activation of peroxymonosulfate to generate $^1\text{O}_2$ with 100% selectivity, *Angew. Chem. Int. Ed.* 60 (2021) 21751–21755.
- [14] X. Zhou, M. Ke, G. Huang, C. Chen, W. Chen, K. Liang, Y. Qu, J. Yang, Y. Wang, F. Li, H. Yu, Y. Wu, Identification of Fenton-like active Cu sites by heteroatom modulation of electronic density, *Proc. Natl. Acad. Sci. U. S. A.* 119 (2022), 2119492119.
- [15] X. Mi, P. Wang, S. Xu, L. Su, H. Zhong, H. Wang, Y. Li, S. Zhan, Almost 100% peroxymonosulfate conversion to singlet oxygen on single-atom CoN_{2+2} sites, *Angew. Chem. Int. Ed.* 60 (2021) 4588–4593.
- [16] Q. Ji, Y. Wang, Y. Lu, W. Yan, F. Hu, W. Zhang, Z. Sun, Z. Qi, L. Song, S. Wei, Single-atom-layer catalysis in a MoS_2 monolayer activated by long-range ferromagnetism for the hydrogen evolution reaction: Beyond single-atom catalysis, *Angew. Chem. Int. Ed.* 60 (2021) 7251–7258.
- [17] W.J. Newsome, S. Ayad, J. Cordova, E.W. Reinheimer, A.D. Campiglia, J.K. Harper, K. Hanson, F.J. Uribe-Romo, Solid state multicolor emission in substitutional solid solutions of metal-organic frameworks, *J. Am. Chem. Soc.* 141 (2019) 11298–11303.
- [18] J. Yang, J.C. Russell, S. Tao, M. Lessio, F. Wang, A.C. Hartnett, S.R. Peurifoy, E. A. Doud, E.S. O'Brien, N. Gadjieva, D.R. Reichman, X. Zhu, A.C. Crowther, S.J. L. Billinge, X. Roy, M.L. Steigerwald, C. Nuckolls, Superatomic solid solutions, *Nat. Chem.* 13 (2021) 607–613.
- [19] J. Wei, F.L. Meng, T. Li, T. Zhang, S. Xi, W.L. Ong, X.Q. Wang, X. Zhang, M. Bosman, G.W. Ho, Spontaneous atomic sites formation in wurtzite CoO nanorods for robust CO_2 photoreduction, *Adv. Funct. Mater.* (2021), 2109693.
- [20] M. Kohantorabi, G. Moussavi, S. Giannakis, A review of the innovations in metal- and carbon-based catalysts explored for heterogeneous peroxymonosulfate (PMS) activation, with focus on radical vs. non-radical degradation pathways of organic contaminants, *Chem. Eng. J.* 411 (2021), 127957.
- [21] X. Feng, R. Zheng, C. Gao, W. Wei, J. Peng, R. Wang, S. Yang, W. Zou, X. Wu, Y. Ji, H. Chen, Unlocking bimetallic active sites via a desalination strategy for photocatalytic reduction of atmospheric carbon dioxide, *Nat. Commun.* 13 (2022) 2146.
- [22] Z. Chen, Y. Fang, L. Wang, X. Chen, W. Lin, X. Wang, Remarkable oxygen evolution by Co-doped ZnO nanorods and visible light, *Appl. Catal. B: Environ.* 296 (2021), 120369.
- [23] Z. Xia, H. Zhang, K. Shen, Y. Qu, Z. Jiang, Wavelet analysis of extended X-ray absorption fine structure data: Theory, application, *Phys. B.* 542 (2018) 12–19.
- [24] H. Li, Z. Zhao, J. Qian, B. Pan, Are free radicals the primary reactive species in Co (II)-mediated activation of peroxymonosulfate? new evidence for the role of the Co (II)-peroxymonosulfate complex, *Environ. Sci. Technol.* 55 (2021) 6397–6406.
- [25] Y. Gao, T. Wu, C. Yang, C. Ma, Z. Zhao, Z. Wu, S. Cao, W. Geng, Y. Wang, Y. Yao, Y. Zhang, C. Cheng, Activity trends and mechanisms in peroxymonosulfate-assisted catalytic production of singlet oxygen over atomic Metal-N-C catalysts, *Angew. Chem. Int. Ed.* 60 (2021) 22513–22521.
- [26] Q. Zhao, X.-H. Yi, C.-C. Wang, P. Wang, W. Zheng, Photocatalytic Cr(VI) reduction over MIL-101(Fe)- NH_2 immobilized on alumina substrate: From batch test to continuous operation, *Chem. Eng. J.* 429 (2022), 132497.
- [27] L. Liu, Z. Liu, H. Bai, D.D. Sun, Concurrent filtration and solar photocatalytic disinfection/degradation using high-performance Ag/TiO_2 nanofiber membrane, *Water Res.* 46 (2012) 1101–1112.
- [28] C. Chu, J. Yang, X. Zhou, D. Huang, H. Qi, S. Weon, J. Li, M. Elimelech, A. Wang, J. H. Kim, Cobalt single atoms on tetrapyrromacrocyclic support for efficient peroxymonosulfate activation, *Environ. Sci. Technol.* 55 (2021) 1242–1250.
- [29] H. Wu, X. Xu, L. Shi, Y. Yin, L.C. Zhang, Z. Wu, X. Duan, S. Wang, H. Sun, Manganese oxide integrated catalytic ceramic membrane for degradation of organic pollutants using sulfate radicals, *Water Res.* 167 (2019), 115110.
- [30] C. Meng, B. Ding, S. Zhang, L. Cui, K.K. Ostrikov, Z. Huang, B. Yang, J.H. Kim, Z. Zhang, Angstrom-confined catalytic water purification within Co-TiO_x laminar membrane nanochannels, *Nat. Commun.* 13 (2022) 4010.
- [31] Z. Lu, G. Zhou, B. Li, Y. Xu, P. Wang, H. Yan, M. Song, C. Ma, S. Han, X. Liu, Heterotopic reaction strategy for enhancing selective reduction and synergistic oxidation ability through trapping Cr(VI) into specific reaction site: A stable and self-cleaning ion imprinted CdS/HTNW photocatalytic membrane, *Appl. Catal. B: Environ.* 301 (2022), 120787.
- [32] H. Li, N. Yuan, J. Qian, B. Pan, Mn_2O_3 as an electron shuttle between peroxymonosulfate and organic pollutants: The dominant role of surface reactive Mn(IV) species, *Environ. Sci. Technol.* 56 (2022) 4498–4506.
- [33] X. Zhao, X. Li, Z. Zhu, W. Hu, H. Zhang, J. Xu, X. Hu, Y. Zhou, M. Xu, H. Zhang, G. Hu, Single-atom Co embedded in BCN matrix to achieve 100% conversion of peroxymonosulfate into singlet oxygen, *Appl. Catal. B: Environ.* 300 (2022), 120759.
- [34] X. Zhang, J. Liu, X. Zheng, R. Chen, M. Zhang, Z. Liu, Z. Wang, J. Li, Activation of oxalic acid via dual-pathway over single-atom Fe catalysts: Mechanism and membrane application, *Appl. Catal. B: Environ.* 321 (2023), 122068.
- [35] H. Zhang, C. Li, L. Lyu, C. Hu, Surface oxygen vacancy inducing peroxymonosulfate activation through electron donation of pollutants over cobalt-zinc ferrite for water purification, *Appl. Catal. B: Environ.* 270 (2020), 118874.
- [36] S. Guo, H. Wang, W. Yang, H. Fida, L. You, K. Zhou, Scalable synthesis of Ca-doped $\alpha\text{-Fe}_2\text{O}_3$ with abundant oxygen vacancies for enhanced degradation of organic pollutants through peroxymonosulfate activation, *Appl. Catal. B: Environ.* 262 (2020), 118250.
- [37] S. Sun, C. Shan, Z. Yang, S. Wang, B. Pan, Self-enhanced selective oxidation of phosphonate into phosphate by $\text{Cu(II)/H}_2\text{O}_2$: Performance, mechanism, and validation, *Environ. Sci. Technol.* 56 (2022) 634–641.
- [38] X. Duan, H. Sun, Y. Wang, J. Kang, S. Wang, N-doping-induced nonradical reaction on single-walled carbon nanotubes for catalytic phenol oxidation, *ACS Catal.* 5 (2014) 553–559.
- [39] N. Amaly, A.Y. El-Moghazy, N. Nitin, G. Sun, P.K. Pandey, Synergistic adsorption-photocatalytic degradation of tetracycline by microcrystalline cellulose composite aerogel doped with montmorillonite hosted methylene blue, *Chem. Eng. J.* 430 (2022), 133077.
- [40] Q. Shi, Y. Zhang, D. Sun, S. Zhang, T. Tang, X. Zhang, S. Cao, Bi_2O_3 -sensitized TiO_2 hollow photocatalyst drives the efficient removal of tetracyclines under visible light, *Inorg. Chem.* 59 (2020) 18131–18140.
- [41] Q. Zhu, B. Qiu, H. Duan, Y. Gong, Z. Qin, B. Shen, M. Xing, J. Zhang, Electron directed migration cooperated with thermodynamic regulation over bimetallic $\text{NiFeP/g-C}_3\text{N}_4$ for enhanced photocatalytic hydrogen evolution, *Appl. Catal. B: Environ.* 259 (2019), 118078.
- [42] J. Lan, M. Luo, J. Han, M. Peng, H. Duan, Y. Tan, Nanoporous B_{13}C_2 towards highly efficient electrochemical nitrogen fixation, *Small* 17 (2021), 2102814.